AGU PUBLICATIONS

Water Resources Research

RESEARCH ARTICLE
10.1002/2016WR018712

Key Points:
- Extreme precipitation occurrence over the western U.S. relates well to a paleo-reconstruction of PDSI
- The primary modes of variability for extreme precipitation occurrences and PDSI relate very well
- The risk of extreme precipitation occurrence can be reconstructed for individual sites

Supporting Information:
- Supporting Information S1

Correspondence to:
S. Steinschneider,
scottsteinschneider@gmail.com

Citation:
Steinschneider, S., M. Ho, E. R. Cook, and U. Lall (2016), Can PDSI inform extreme precipitation?: An exploration with a 500 year long paleoclimate reconstruction over the U.S., *Water Resour. Res.*, *52*, 3866–3880, doi:10.1002/2016WR018712.

Received 31 JAN 2016
Accepted 22 APR 2016
Accepted article online 28 APR 2016
Published online 22 MAY 2016

Can PDSI inform extreme precipitation?: An exploration with a 500 year long paleoclimate reconstruction over the U.S.

Scott Steinschneider[1], Michelle Ho[2], Edward R. Cook[3], and Upmanu Lall[1]

[1]Department of Earth and Environmental Engineering, Columbia University, New York, New York, USA, [2]Columbia Water Center, Columbia University, New York, New York, USA, [3]Tree Ring Lab, Lamont-Doherty Earth Observatory, Palisades, New York, USA

Abstract This study explores whether it is possible to reconstruct the frequency of extreme precipitation occurrence across the contiguous United States (CONUS) using the Living Blended Drought Atlas (LBDA), a 500 year paleoclimate reconstruction of the summer (June–August) Palmer Drought Severity Index (PDSI). We first identify regions of the country where the LBDA may reflect the occurrence of extremes based on their seasonality and contribution to total annual moisture delivery. Correlation measures are used to assess the relationship between the frequencies of extreme precipitation occurrence and both the instrumental monthly PDSI and the annual LBDA-estimated PDSI. Extreme precipitation is found to account for a large portion of total precipitation west of the Mississippi River and clusters in particular seasons (winter and summer), supporting a strong relationship with the LBDA without much information loss from the instrumental PDSI data. Dimension reduction techniques are used to explore the joint spatiotemporal structure of extreme precipitation occurrence and LBDA across the country. The primary modes of variability of the LBDA and extreme precipitation occurrence relate remarkably well for a region centered over the southwest that exhibits an ENSO-like time-frequency structure. Generalized linear models (GLMs) are used to demonstrate the feasibility of reconstructing the annual extreme precipitation frequency over the 500 year prehistoric record at two sites in the southwest and Southern Plains. GLM-based reconstructions show a high degree of structured variability in the likelihood of extreme precipitation occurrences over the prehistoric record.

1. Introduction

Our understanding of decadal to centennial and longer-scale variations in extreme precipitation is severely limited by the lack of multicentennial instrumental rainfall data. While reconstructions of drought, temperature, and streamflow are routinely developed using a variety of proxies (e.g., tree rings, corals, and ice cores), no such efforts have been directed at the reconstruction of extreme rainfall given the perceived incompatibility between the temporal scale of events and the sensitivity of paleoclimate proxies. However, it is possible that the occurrence of extreme rainfall could be inferred in regions where (1) rainfall-sensitive paleoclimate records exist and (2) seasonal or annual rainfall totals are dominated by a few extreme rainfall events. Across much of North America, one such paleoclimate proxy is available through the Living Blended Drought Atlas (LBDA) [*Cook et al.*, 2010], a multicentennial tree ring-based paleoclimate reconstruction of the Palmer Drought Severity Index (PDSI) [*Palmer*, 1965]. The PDSI records both positive and negative excursions in moisture availability related to periods of high and low rainfall that may also be captured in the tree ring-based LBDA. This leads to the key question posed in this paper as to whether the LBDA contains useful information about extreme precipitation occurrence in any region. We find affirmative evidence in support of this conjecture over a large part of the contiguous United States (CONUS) and show that these regions coincide with areas where rainfall totals are heavily influenced by a few extreme rainfall events during seasons important for moisture availability for tree growth. We explore how the spatiotemporal structure of extreme precipitation and PDSI are related using the LBDA records and investigate links to larger-scale oscillations in the climate system. The ability to reconstruct extreme precipitation occurrence using the LBDA is demonstrated for two selected locations where we use generalized linear models (GLMs) with the instrumental records of extreme precipitation frequency in a water year, and the instrumental PDSI corresponding to the LBDA reconstruction, and use this fitted model to project extreme precipitation frequency over the

500 year record. Structured variations in the reconstructions are explored and prospects for the application of such methods utilizing the original tree ring series rather than the LBDA are discussed.

2. Background

There has been substantial progress over the last several decades in our understanding of historic hydroclimate variability across the CONUS [*Namias*, 1966; *Ropelewski and Halpert*, 1987; *Trenberth et al*., 1988; *Piechota and Dracup*, 1996; *Gershunov and Barnett*, 1998; *Barlow et al*., 2001; *McCabe et al*., 2004; *Goodrich*, 2007; *McCabe et al*., 2008], and dynamic climate modeling has enabled attribution studies to link droughts and pluvials on multiannual to decadal time scales with large-scale ocean-atmosphere mechanisms in the Pacific and Atlantic Oceans [*Wang et al*., 2008; *Schubert et al*., 2009; *Kushnir et al*., 2010; *Wang et al*., 2010; *Dai*, 2013; *Seager and Hoerling*, 2014]. Similar lines of work have been pursued for extreme precipitation and flooding events, but with more difficulty [*Zwiers et al*., 2013; *Patricola et al*., 2013; *Sillmann et al*., 2013] due to parameterized, coarse model grids that cannot represent local convection [*Dai*, 2006; *Déqué et al*., 2007; *Kendon et al*., 2012; *Chan et al*., 2014; *Kysely et al*., 2015], and biases in larger-scale storm systems [*Pritchard et al*., 2011; *Daloz et al*., 2012; *Bukovsky et al*., 2013; *Zappa et al*., 2013; *Seiler and Zwiers*, 2015; *Walsh et al*., 2015].

Paleoclimate reconstructions provide an alternative approach to improve our understanding of past hydroclimate variability using archives that preserve signals of environmental variability [*Cronin*, 2010; *Evans et al*., 2013] prior to instrumental or historical (i.e., qualitative) records. A large suite of paleoclimate archive types (e.g., tree rings, ice cores, land and ocean boreholes, and speleothems) has been used as proxy indicators of climate variability and extreme events across the globe [*Jones et al*., 2009]. One key product that has emerged from these studies particular to drought in the CONUS is the Living Blended Drought Atlas (LBDA) [*Cook et al*., 2010], an extension of the seminal North American Drought Atlas [*Cook et al*., 1999; *Cook and Krusic*, 2004]. The LBDA is an amalgamation of 1845 tree ring chronologies into a paleoclimate reconstruction of the summer (June–August) Palmer Drought Severity Index (PDSI) that spans the entire CONUS region for the past 500 years. This product has proven instrumental in understanding the spatiotemporal patterns and likelihood of drought across the CONUS [*Cole et al*., 2002; *Fye et al*., 2003; *Lyon et al*., 2005; *Woodhouse et al*., 2005; *Herweijer et al*., 2006; *Stahle et al*., 2007; *Cook et al*., 2010, 2013, 2014; *Ault et al*., 2014].

Paleoclimate work has also been pursued for extreme wet events, but with more difficulty. Analysis of extreme paleo-hydrologic events has primarily focused on prehistoric floods, using paleostage indicators (PSI) along river reaches or in the floodplain that record the level of past floods [*Benito and Thorndycraft*, 2005]. The use of these data, particularly in bedrock canyon basins in the southwest U.S. [*Baker*, 1977; *Patton and Dibble*, 1982; *Ely and Baker*, 1985; *Enzel et al*., 1993; *Levish*, 2002], has been extremely successful at detecting the threshold exceedance of prehistoric high-magnitude floods. However, unlike the tree rings underlying the LBDA, the availability of paleostage evidence is limited across the country [*Baker*, 2013] and is typically not annually resolved. Furthermore, annually resolved paleoflood evidence (e.g., flood tree rings [*Yanosky*, 1983; *Therrell and Bialecki*, 2015]) is limited due to other factors including biological sensitivity and the extent and timing of the floods [*St*. *George and Nielsen*, 2003].

Given the limited paleoflood evidence across the country and the high uncertainty that underscores extreme event risk assessments, there is a need to augment the prehistoric records of extreme wet events. We explore whether the LBDA, with a high spatial and temporal resolution, can be used for this purpose. An exploration of this potential is the primary contribution of this work. The use of tree ring archives to reconstruct extremes is unlikely to resolve all features of short-duration (i.e., daily) extremes and may, in some regions, be insensitive to any precipitation signal, particularly in humid areas where moisture is less strongly limiting for tree growth. However, the LBDA was amalgamated using only moisture and temperature-sensitive tree ring chronologies. Therefore, the LBDA may provide evidence of a shift in the odds for extreme rainfall and floods in areas where extremes play a large role in moisture delivery and occur in seasons linked to tree growth. Taken in conjunction with other paleoflood evidence (where available), this could advance our understanding of past annual variations in the frequency of extreme events and improve methods for nonstationary flood and extreme rainfall probability estimation, as part of a modern dynamic risk assessment and management approach [*Jain and Lall*, 2001; *Sankarasubramanian and Lall*, 2003; *Kwon et al*., 2008; *Lima and Lall*, 2010; *Delgado et al*., 2014; *Merz et al*., 2014].

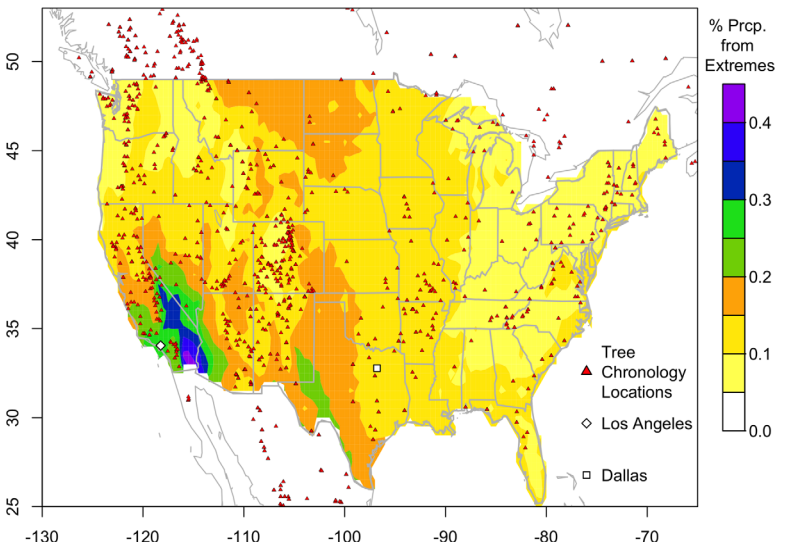

Figure 1. Ratio of cumulative extreme to cumulative total precipitation over the period of record. Tree ring sampling sites for the LBDA, Los Angeles, CA, and Dallas, TX, are also shown.

3. Data

The PDSI, originally developed by *Palmer* [1965], is a monthly measure of the balance between atmospheric moisture supply and demand and takes into account regional climatology and short-term hydrologic persistence. *Heddinghaus and Sabol* [1991] proposed a modified version of the PDSI to enable near-real time monitoring and address discrepancies in the continuity of PDSI when climate transitions between drought and pluvial states. Two versions of the modified PDSI, an instrumental-based record and paleoclimate reconstruction, are used in this analysis. The instrumental PDSI is a monthly record from 1895 to 2005 that spans North America and was derived using station data for precipitation and temperature and a gridded soil water capacity data set interpolated to a 0.5° × 0.5° latitude/longitude grid [*Heim et al*., 2007].

The Living Blended Drought Atlas (LBDA) is a paleoclimate reconstruction of average summer (June–August) PDSI over North America that is spatially complete over the CONUS from 1473 to 2005. The LBDA incorporates information from 1845 tree ring chronologies (see Figure 1) and was calibrated to the PDSI developed by *Heim et al*. [2007]. The reconstruction was formulated to enable the gridded data to be seamlessly updated with instrumental-based records of PDSI and consists of these instrumental records from 1979 onward. *Cook et al*. [2007] demonstrate good agreement between reconstructed and instrumental PDSI records; additional support for this relationship in the period prior to 1979 is presented in the supporting information, as is further information on the tree species used in the development of the LBDA.

Daily precipitation across the CONUS is taken from the CPC U.S. unified precipitation data set [*Chen et al*., 2008]. The continuous precipitation product is derived from gaged data interpolated to a 0.25° grid between 20°N–50°N and 130°W–55°W [*Xie et al*., 2007] and is truncated to span 1 October 1948 to 30 September 2005 in order to run over complete water years. The data are then averaged up to a larger 0.5° × 0.5° grid to match the PDSI and LBDA data. We note that the results presented below are remarkably similar if the data are aggregated to the 0.5° grid level by taking the maximum precipitation value of 0.25° grid cell instead of their average. Daily precipitation data are also gathered for two individual gaging stations (GHCND:USW00023174 Los Angeles International Airport, CA, and GHCND:USW00003927 Dallas Fort Worth WSCMO Airport, TX) through NOAA's Global Historical Climatology Network (GHCN) from 1 October 1948 to 30 September 2005 to demonstrate the reconstruction of prehistoric frequencies of extreme precipitation. Both gages have continuous records over the time period without any missing values.

4. Analysis

In this section, we first explore the moisture contribution and seasonality of extreme precipitation events across the CONUS to better understand the physical basis underscoring a possible link between tree growth

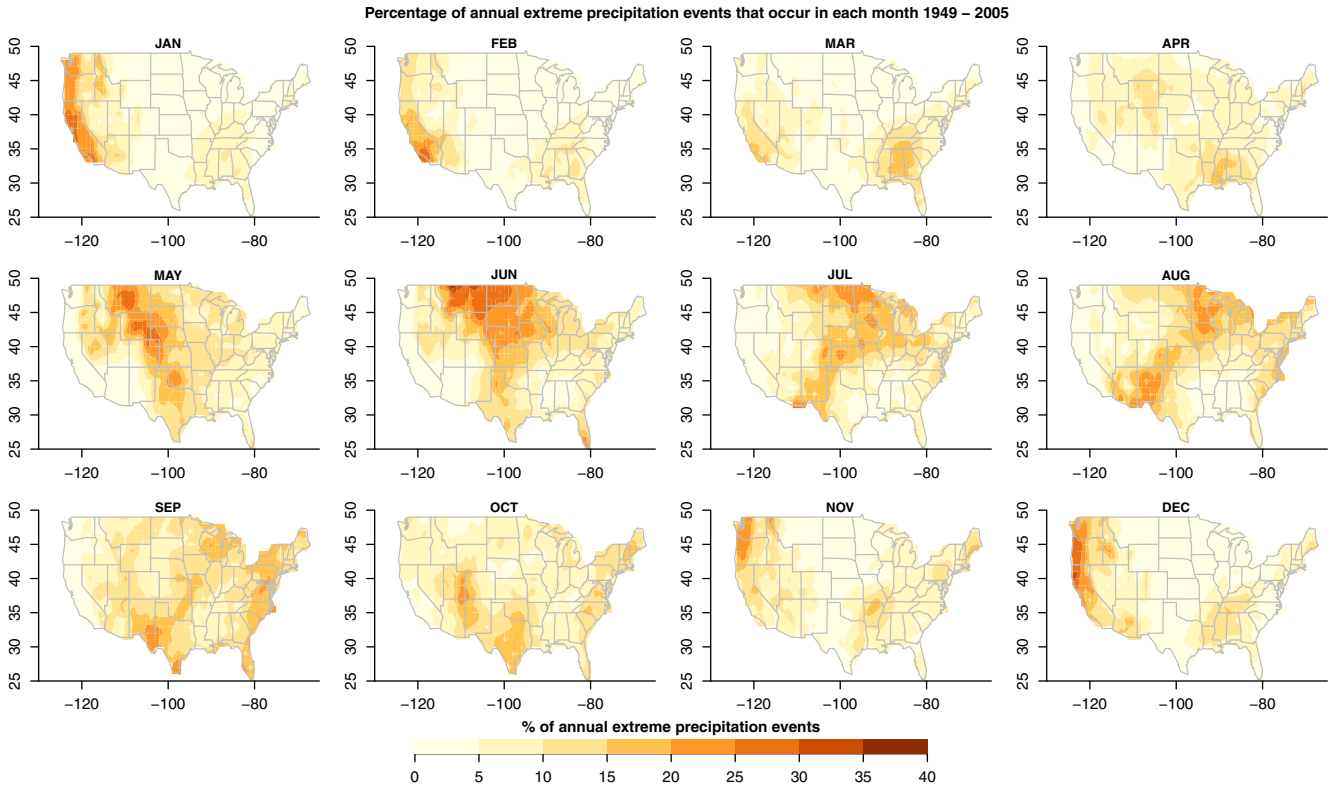

Figure 2. Percentage of extreme precipitation events that occur in each calendar month.

and precipitation extremes. Then, we investigate the relationship between extreme precipitation occurrence and both the instrumental PDSI and LBDA. Next, the joint patterns of spatiotemporal variability in the LBDA and extreme precipitation occurrences are investigated using multiple-dimension reduction techniques and a wavelet coherence analysis. Finally, we demonstrate the potential for annual reconstructions of the frequencies of extreme rainfall for two rainfall-gaging stations based on the LBDA over the 500 year prehistoric period and explore the resulting variability of the reconstructed series using wavelet analysis.

4.1. Extreme Precipitation Occurrence

For each (0.5° × 0.5°) CPC precipitation grid cell, we define the count of extreme precipitation occurrences (hereafter referred to as the peaks-over-threshold (POT) data) using the number of precipitation days in each water year greater than the 99.5th percentile of daily precipitation across all days of the record (including zero precipitation days). This threshold is calculated without seasonal distinction and leads to approximately two extreme events per year on average. No separation was required between individual events, although a sensitivity analysis showed that requiring a 3 day separation between extremes has no material effects on the results of the analysis.

The ratio of cumulative precipitation delivered during extreme events to total precipitation for all events across the entire record is shown in Figure 1. This ratio highlights regions where extreme precipitation contributes a large fraction of the total moisture, and thus where tree ring widths may be more reflective of extremes. The southwest U.S. stands out as a region where extremes dominate moisture delivery, with average contribution exceeding 37% in areas surrounding the Mojave Desert. While not as dramatic as the southwest, a wide swath of the Great Plains spanning from west Texas to Montana and the Western Mountain ranges (Rockies, Cascades, and the Sierra Nevada) also show high moisture contributions from extremes.

The seasonality of the POT data, reported as the percentage of events by calendar month, is examined to identify extreme event clustering in months that are more likely to be linked to tree ring widths (Figure 2). As documented elsewhere [*Kunkel et al.*, 1999; *Groisman et al.*, 2001], the U.S. West Coast receives the

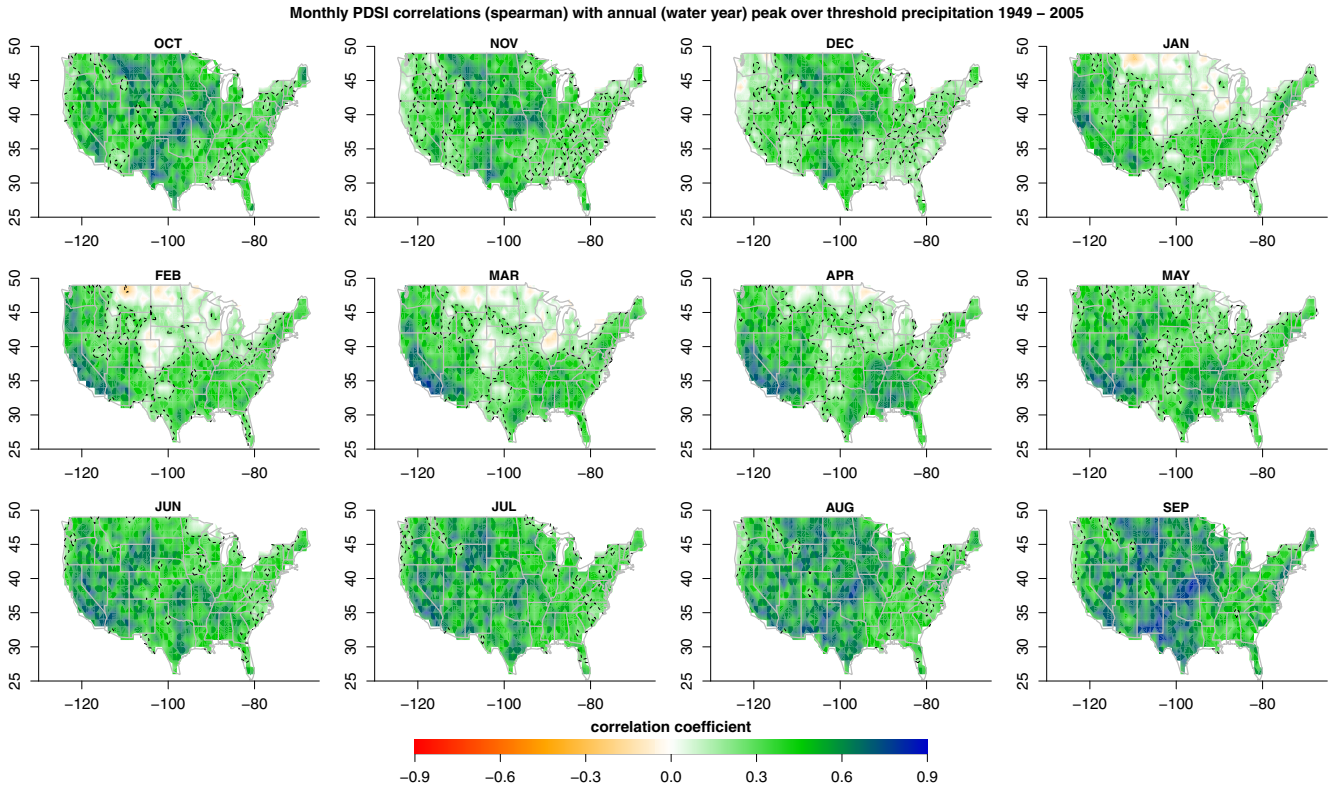

Figure 3. Spearman correlation coefficients between the number of annual water year (October–September) extreme precipitation events and monthly, instrumental PDSI.

majority of extremes during the winter (November–March), while the summertime (June–September) Southwest Monsoon also accounts for a large portion of extremes in Arizona, New Mexico, and west Texas. Heavy precipitation in the Great Plains clusters from late spring through the summer (May–August), with a northern core region that migrates from Wyoming to Wisconsin as the season progresses. Extremes are more spread out during the year across the broader eastern U.S., albeit with minor peaks in the southeast between March–April and both the southeast and northeast during the summer (June–September).

Since tree growth and the PDSI are influenced by short-term hydrologic persistence and are reflective of recent moisture conditions, it is likely that the reconstruction of extreme precipitation occurrence using the LBDA will be most skillful in regions where climate mechanisms like the Great Plains Low Level Jet in the central U.S. [*Higgins et al*., 1997] and the North American Monsoon in the southwest U.S. [*Bukovsky et al*., 2013] drive extremes and annual rainfall totals during or shortly prior to the summertime growing season. In addition, winter precipitation west of the Rocky Mountains can also relate to summer PDSI, LBDA, and tree growth [*Fritts*, 1976; *Woodhouse and Meko*, 1997; *St. George et al*. 2010], where the accumulation of snow during extreme winter weather acts as a reservoir that continues to deliver moisture from spring onward [*Rochefort et al*., 1994; *McNamara et al*., 2005]. The seasonality of extreme precipitation events taken in tandem with their contributions to annual precipitation totals suggests that the best relationships between the LBDA and extreme precipitation occurrence are most likely located in the western half of the United States, and particularly in the southwest. These relationships are explored next.

4.2. Relationship Between the LBDA and Extreme Precipitation

We first consider the relationship between the number of extreme events and the instrumental PDSI between 1948 and 2005. These relationships are explored on a monthly basis using nonparametric Spearman (rank) correlations between the annual POT data and monthly PDSI of the corresponding calendar year on a grid cell by grid cell basis (Figure 3). The frequency of extreme precipitation events over a water year is significantly correlated with the instrumental PDSI at the 99% level for individual, grid-by-grid tests over most of the CONUS between May and October. Correlations also exhibited field significance at the 0.01 level for all months based on the false discovery rate adjusted p value [*Benjamini and Hochberg*, 1995].

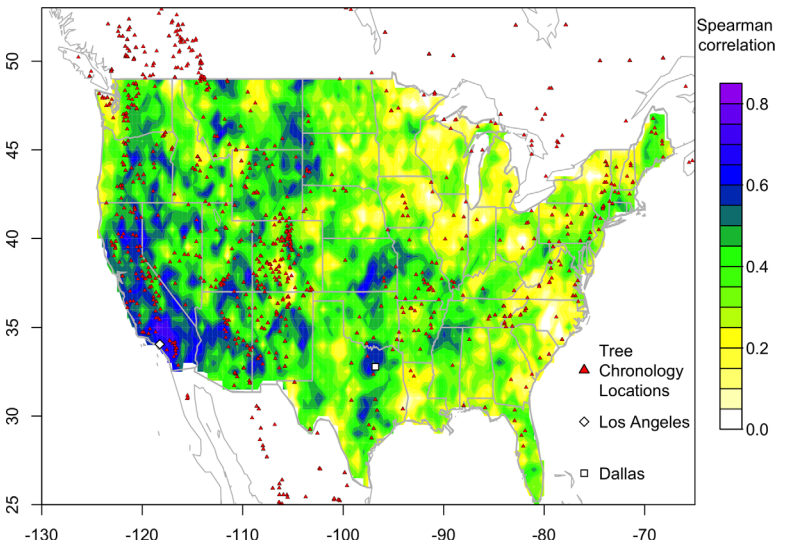

Figure 4. Grid-level Spearman correlation coefficients between LBDA values and the number of extreme precipitation events in each water year. Tree ring sampling sites for the LBDA, Los Angeles, CA, and Dallas, TX are also shown.

The correlation patterns are unchanged if Pearson or Kendall correlation coefficients are used instead (not shown), although the magnitudes are the largest when using Pearson correlations, indicating that the relationship is somewhat stronger in the tails of the PDSI and POT data than in the center of the distribution.

The significant relationships over the boreal summer are promising for the reconstruction of the frequencies of extreme precipitation based on the LBDA. A large proportion of extreme precipitation events in the central south CONUS, near New Mexico and Texas, occur during the North American Monsoon in July, August, and September and are correlated with PDSI in these months. High correlations are also found during the summer (June–September) throughout the northern Great Plains, likely linked to moisture delivery by the Great Plains Low Level Jet. In contrast, extreme precipitation events farther west (western Arizona, southern California, and broadly the western coastline) are correlated with winter PDSI values, but also strongly correlated with PDSI later in the year during spring and summer. The seasonality of extreme precipitation and its relationship with PDSI in the spring and summer tree-growing season corroborates with previous findings that tree growth in the southwestern and western CONUS is influenced by winter precipitation [*Fritts*, 1976; *Woodhouse and Meko*, 1997; *St. George et al.*, 2010]. In the eastern U.S., some highly significant correlations are present in the southeast during the spring (March–April), but overall the signal between the POT and PDSI data is weaker east of the Mississippi River. In summary, much of the potential skill for explaining extreme precipitation occurrences lies in the central and western U.S. and can be derived from PDSI values in the summer (June–August), suggesting that the LBDA is capturing much of the PDSI-extreme precipitation relationship, although further improvements are likely possible throughout the Great Plains if the LBDA were extended to account for September PDSI values.

Figure 4 shows the Spearman correlation coefficients between the annual POT data and the annual LBDA over the period 1948–2005 and on a grid cell by grid cell basis. These relationships directly indicate the potential for extreme precipitation reconstruction. However, since the LBDA includes instrumental data from 1979 onward, we also note that the correlations in Figure 4 remain relatively unchanged, particularly in the West, if recalculated over only the 1948–1978 (tree ring only) period. The correlation coefficients in Figure 4 are significant at the 0.01 level on a grid-by-grid basis over much of the CONUS, with a median of 0.36 and interquartile range of [0.27,0.45]. Correlations also exhibited field significance at the 0.01 level, and the patterns are invariant when a Kendall or Pearson correlation coefficient is used. The relationships are the strongest in southern California and western Nevada, as well as in patches throughout the Great Plains, with correlations often exceeding 0.5 and reaching as high as 0.80. We note that further improvements in this relationship are likely possible throughout the Great Plains if the LBDA was extended to account for September PDSI values, as suggested by Figure 3. Overall, much of the western U.S. shows promise for the reconstruction of extreme precipitation occurrences based on the current LBDA.

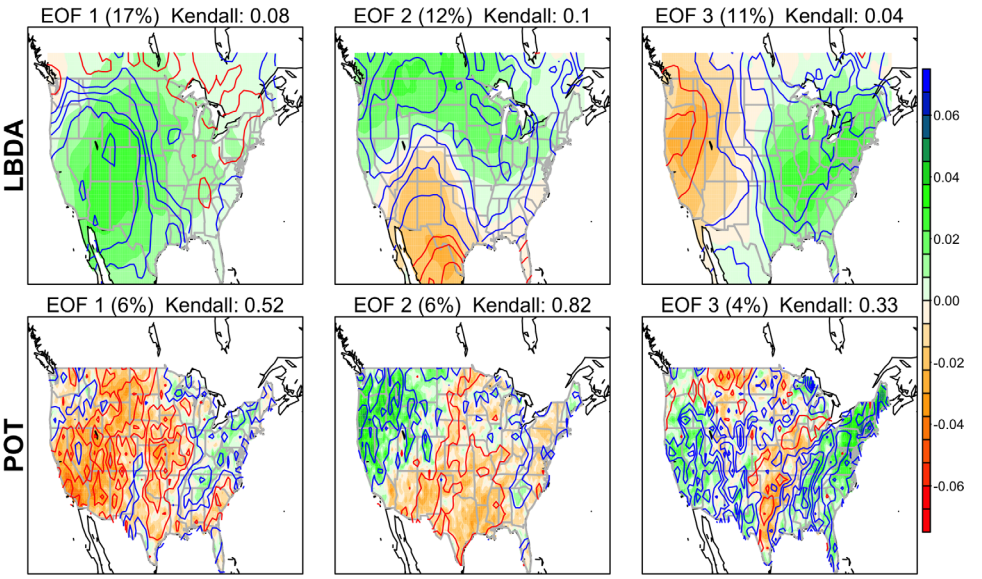

Figure 5. Loading patterns for the leading three EOFs (shaded) and associated archetypes (contours) of the (top row) LBDA and (bottom row) POT data. Note that unlike EOFs, the archetypes have no natural ordering by degree of variability explained. The variance explained by each EOF is given in the title, as well as the Kendall correlation between its principal component and associated archetype time projection. Positive (blue) and negative (red) contours are given in increments of 0.5.

4.3. Comparing POT and LBDA Spatiotemporal Variability

Figure 4 shows moderate to strong relationships between the LBDA and extreme precipitation occurrence on a local (grid-cell) basis for much of the western CONUS, but we are also interested in whether these data exhibit similar spatiotemporal variability on a larger scale. Methods of dimension reduction such as Empirical Orthogonal Functions (EOFs) and rotated EOFs (REOFs) are often used to extract the main modes of variability of climate fields [*Hannachi et al.*, 2007]. However, the orthogonality constraints imposed on EOF analysis can result in spurious Buell patterns characterized by overly complex polar structures inconsistent with the data, while REOFs can result in oversimplified structures that ignore complexity in the original field [*Wilks*, 2011]. For this reason, we also use Archetype Analysis (AA) [*Cutler and Breiman*, 1994; *Stone and Cutler*, 1996; *Steinschneider and Lall*, 2015] in addition to traditional EOF and REOF methods to verify the spatial patterns identified in the EOF analysis.

AA is a complementary algorithm to EOF analysis that similarly decomposes the spatiotemporal variability of a climate field but with different underlying constraints. AA represents each time-based observation of a climate field as a convex combination of a limited set of archetypes, or (possibly unobserved) extremal points lying on the boundary of the convex hull of the original data set. The archetypes themselves are constrained to be a convex combination of the original data and can be interpreted as pure types or characteristic extremal spatial patterns. Similar to EOF and REOF analysis, AA produces spatial loading patterns and time series projections of those patterns analogous to EOFs and principal components (PCs). For details regarding the mathematical formulation and fitting algorithms of AA, we refer the reader to the references above [see *Cutler and Breiman*, 1994; *Stone and Cutler*, 1996; *Steinschneider and Lall*, 2015]. The important point to note is that the spatial loading patterns of AA do not have orthogonality constraints like EOFs and are either actual observations or convex mixtures of observations, which eases their interpretation and makes them useful for comparing and evaluating the fidelity of EOF and REOF patterns.

The EOFs, REOFs (Varimax rotation), and archetypes are computed for both LBDA and POT climate fields. Initially, the number of retained EOFs, REOFs, and archetypes are (5,8,5) for the LBDA data and (5,7,5) for the POT data; these values were selected using North's Rule [*North et al.*, 1982] (EOFs), scree tests (archetypes), and a trial-and-error procedure based on the stability of the leading eigenvectors (REOFs) [*Wilks*, 2011] (see supporting information). For brevity, in Figure 5, we only show the loading patterns of the first three leading EOFs for the LBDA (top row) and POT data (bottom row). We also show the associated archetypes that have similar loading patterns and high correlations between the respective time projections. We note that the

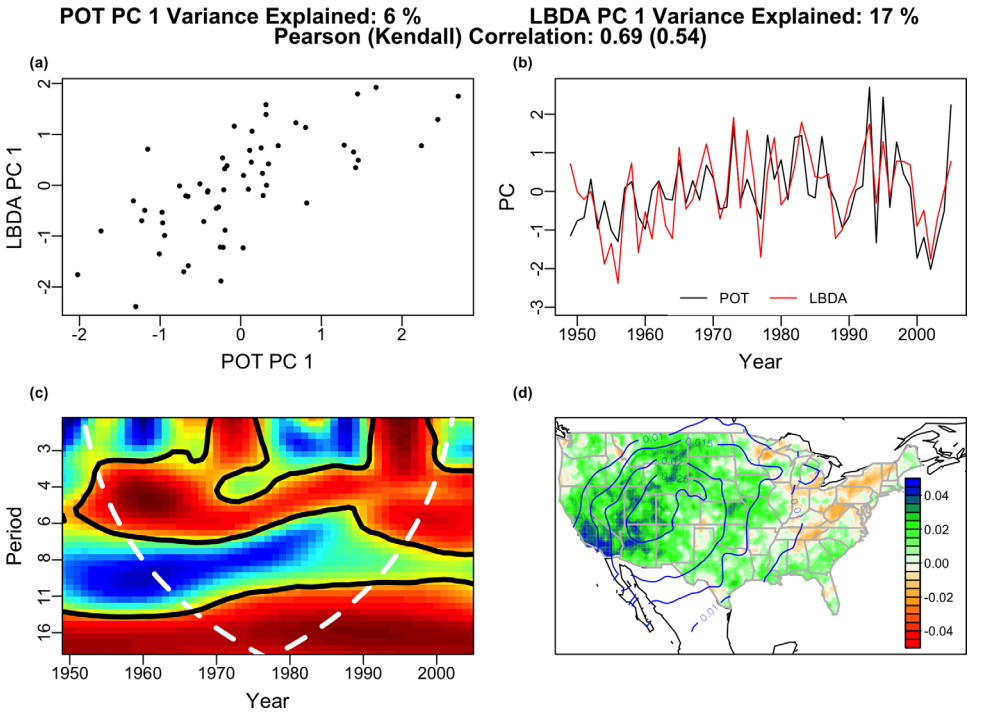

Figure 6. Comparison of EOF1 of the LBDA and POT data, including (a) scatterplot of PCs, (b) time series plots of PCs, (c) wavelet coherence (significance is outlined in bold at the 90% level), and (d) their loading patterns (LBDA contoured, POT shaded). Contours are shown at 0.05 increments. The variance explained by both EOFs and their Pearson and Kendall correlation coefficients are also given.

relatively low variance explained by the EOFs for both LBDA and POT data sets is likely related to the size of the study domain and for the POT data, the level of heterogeneity in extremes. The archetype loadings for the POT data are also more variable due to this heterogeneity and the constraint that archetype patterns be convex combinations of actual observations.

For the LBDA, the first EOF shows a monopole over most of the western U.S., followed by north-south and east-west dipoles for EOF2 and EOF3. The monopole and dipole structures in the first few EOFs are usually indicative of spurious Buell patterns caused by orthogonality constraints [*Wilks*, 2011]. However, the archetypes generally reflect these same configurations, and since archetypes have no orthogonality constraints and are more likely to resemble actual observations in the data set, this supports the fidelity of the identified patterns. We have further confidence in these dipole patterns after viewing animations of instrumental monthly PDSI data (http://www.ncdc.noaa.gov/temp-and-precip/drought/historical-palmers/) and seeing similar patterns emerge consistently. Similar arguments support the first three EOFs of the POT data. After comparing the spatial loadings of all retained EOFs with those of all retained archetypes for the LBDA and POT data, and repeating a similar analysis for the REOFs (see supporting information), the EOFs were determined to be more consistent with the archetypes than the REOFs and are thus more likely to actually represent the spatiotemporal variability of the data. As such, the EOFs were selected for further analysis.

Figure 6 shows a comparison between the leading EOF of the LBDA and POT data. The comparisons include a visual evaluation of their loading patterns, time projections, and a wavelet coherence analysis [*Torrence and Compo*, 1998; *Grinsted et al.*, 2004] to examine the time-frequency relationships between PCs. The first EOFs of the LBDA and POT data relate remarkably well. Both patterns are centered over the southwestern U.S., although EOF1 for the POT data also has a slightly opposing loading pattern over the Ohio River Basin. Neither PC shows a substantial trend, but they are significantly correlated with a Kendall (Pearson) correlation coefficient of 0.53 (0.69). Both PCs also show significant oscillations in the 4–6 and 11–16 year frequency bands. Given past work on the LBDA [*Rajagopalan et al.*, 2000; *Cole et al.*, 2002], the 4–6 year oscillation is likely an El Niño-Southern Oscillation (ENSO) signal that also propagates into the extremes of the southwest [*Trenberth et al.*, 1988; *Piechota and Dracup*, 1996; *Ward et al.*, 2014], while decadal fluctuations in ENSO [*Gershunov and Barnett*, 1998; *Barlow et al.*, 2001; *Goodrich*, 2007] may also explain the

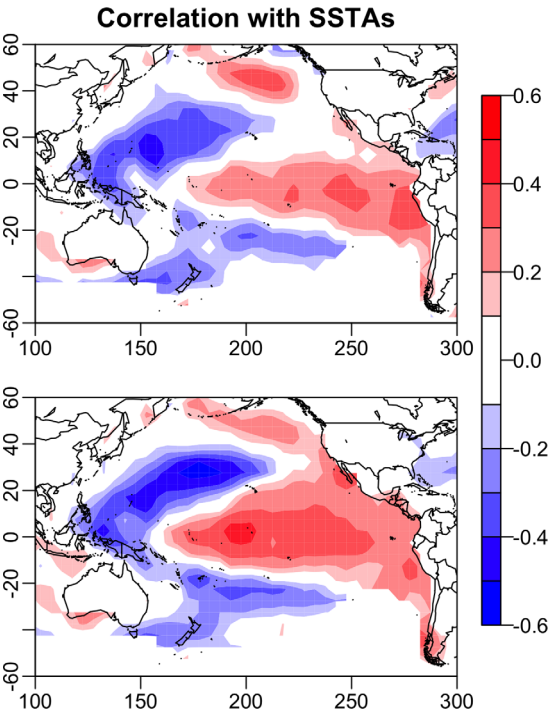

Figure 7. Pearson correlations between detrended SSTAs and PC1 of the (top) LBDA and (bottom) POT data. Absolute correlations above 0.27 are significant at the 0.05 level.

significant signal in the 11–16 year band, although such decadal structure has also been identified in precipitation records in regions not often influenced by ENSO conditions [*Markonis and Koutsoyiannis*, 2015].

To better understand the link to ENSO, Figure 7 shows the correlations between detrended, winter (DJFM) sea surface temperature anomalies (SSTAs) and the first PC of both the LBDA and POT data. Both PCs exhibit a positive relationship with ENSO. Interestingly, though, the relationship with the POT data appears stronger and centered farther into the central Pacific (Niño 3.4 region), while the core region of correlations is weaker and shifted farther east (Niño 1.2 region) for the LBDA. The shift in SST region is likely due to differences in the spatial distribution of loadings for the POT and LBDA EOFs. The loading patterns for the POT are focused strongly in the southwest while those for the LBDA are spread farther toward the central plains. This is similar to the shift in the core region of correlations between gridded, winter (DJFM) average precipitation and ENSO when changing from a Niño 3.4 to Niño 1.2 index (not shown). The link between wintertime precipitation extremes in the southwest and ENSO is well understood [*Cayan et al*., 1999] and underscores the strong relationship seen in Figure 7. PC1 of the LBDA, being a summertime index centered in the southwest, has been linked to extreme precipitation through the snow accumulation from (often extreme) wintertime storms [*Fritts*, 1976; *Woodhouse and Meko*, 1997; *St. George et al*., 2010]. We speculate that ENSO and the LBDA are indirectly linked through wintertime snow accumulation and melt, with extreme wintertime precipitation events acting as a bridge. Further validation of this hypothesis requires an in-depth analysis of snow records and the possible relationship between wintertime ENSO and the summertime Southwest Monsoon [*Wang et al*., 2012] that is beyond the scope of this work and is thus suggested for further research.

Overall, the remarkable similarities shared by the primary modes of spatiotemporal variability of both POT and LBDA data sets—namely their in-phase inter-annual and decadal fluctuations across the western United States—suggest persistent, anticorrelated risk of droughts and extreme precipitation across the region that may be somewhat predictable based on seasonal forecasts of ENSO. This structure could be very relevant for planning and management activities that often occur on these inter-annual and decadal time scales.

4.4. Reconstruction of the Frequency of Extreme Precipitation With Generalized Linear Models

As an example of the potential for using the LBDA data for insights into long-term fluctuations of the frequency of occurrence of extreme precipitation, GLMs are used to estimate the relationship between the average occurrence rate of extremes and the instrumental PDSI and then reconstruct the distribution of extreme precipitation occurrences into the prehistoric record using the LBDA. Here we assume that all substantive fluctuations in extreme precipitation average occurrence rates can be represented by variability in the LBDA data. The reconstruction is applied to two rainfall gages in the southwest U.S. (Los Angeles, CA) and Southern Plains (Dallas, TX). A Poisson regression is used to estimate the rate (annual frequency) of extreme precipitation occurrence using a logistic link function $\lambda(PDSI_t)$ of a regional PDSI indicator, taken as the $0.5^\circ \times 0.5^\circ$ instrumental PDSI grid cell in which the precipitation station is located. In practice, one could consider a more formal process for the selection of a PDSI neighborhood to inform such a regression. Here for demonstration purposes, a simpler approach is used.

Table 1. The Distribution of *p* Values for the Likelihood Ratio Tests Across the 1000 Training and Testing Sets for Both the Los Angeles, CA, and Dallas, TX, Gages

	Los Angeles, CA, Station		Dallas, TX, Station	
Percentile	Training	Testing	Training	Testing
1%	<0.01	<0.01	<0.01	<0.01
5%	<0.01	<0.01	<0.01	<0.01
10%	<0.01	<0.01	<0.01	<0.01
25%	<0.01	<0.01	<0.01	<0.01
50%	<0.01	<0.01	<0.01	<0.01
75%	<0.01	<0.01	<0.01	<0.01
90%	0.02	0.04	0.02	0.05
95%	0.06	1	0.03	0.3
99%	0.40	1	0.14	1

The model calibration is first verified using a leave-k-out cross-validation procedure over the instrumental record using likelihood ratio tests. In this procedure, k = 28 years of data (half the record) are randomly removed from the record and both the Poisson regression and a standard maximum likelihood estimator is fit to the remaining data. A likelihood ratio test is then used to compare the two models over both the training and testing sets. This process is repeated 1000 times, and the distribution of *p* values from the likelihood ratio test is examined to determine if the Poisson regression provides robust improvement over the null model (Table 1). For the Los Angeles, CA, gage, the *p* values from the likelihood ratio tests are at less than the 0.05 level for almost 95% of the training sets and for 90% of the testing sets, suggesting that that the Poisson regression model significantly outperforms the baseline Poisson model. The Poisson regression model performs similarly against the null model for the Dallas, TX, gage, with the *p* value below the 0.05 level in more than 95% of the training sets and almost 90% of the testing sets. Overall, the Poisson regression model provides a robust improvement over a null Poisson fit for both the Los Angeles, CA, and Dallas, TX, gages.

After verifying the skill of the Poisson regression model, it is used to reconstruct the mean rate of extreme precipitation occurrences for the prehistoric period at both sites (Figure 8). The mean parameter estimate is shown along with 90% confidence bounds. During the instrumental period (1895–2005), these bounds are

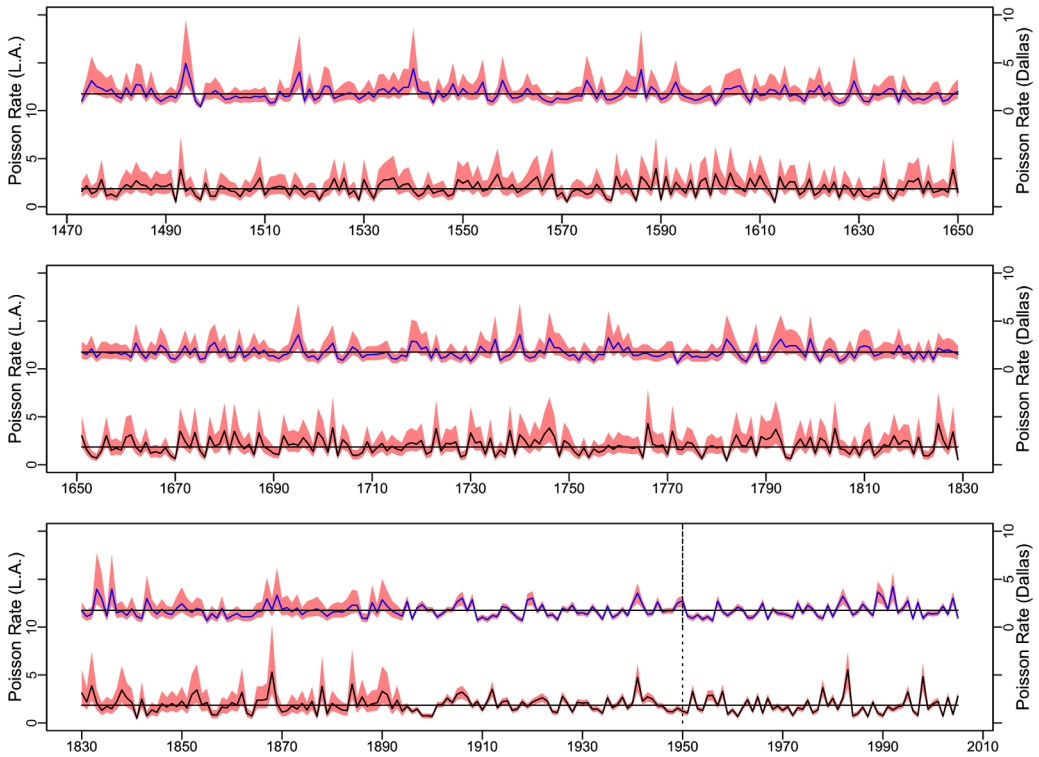

Figure 8. Reconstructed mean Poisson rate based on the LBDA with 90% confidence bounds for the Los Angeles, CA (black, left axis) and Dallas, TX (blue, right axis) precipitation gages. Confidence bounds post-1895 account for regression parameter uncertainty, while pre-1895 they also include uncertainty in the tree ring/PDSI relationship. The beginning of the calibration period is indicated by a vertical dotted line.

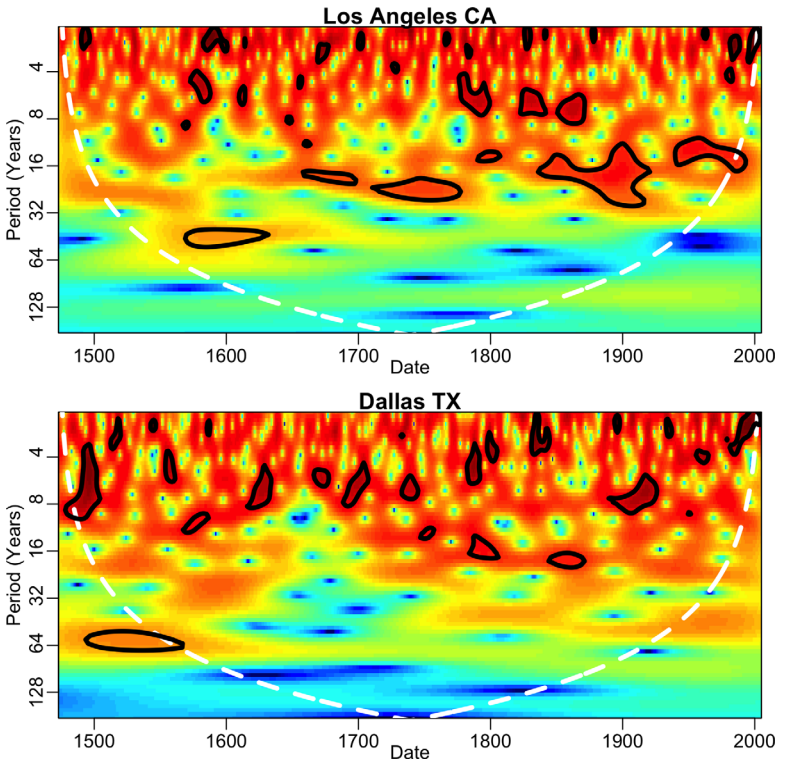

Figure 9. Wavelet spectra for the reconstructed, log-transformed mean Poisson rate parameter for the Los Angeles, CA, and Dallas, TX, precipitation gages.

based entirely on the standard errors of the GLM parameter estimates and are relatively narrow at the reported confidence level. In the preinstrumental period (1473–1894), the uncertainty underlying the LBDA must also be carried through the regression. This is achieved using a Monte Carlo approach. Here sample time series of the PDSI are generated by adding the LBDA values to random deviates with variance equal to the mean squared error of the original PDSI fit for each location, as reported by *Cook et al*. [2007]. Samples of the GLM parameters are also generated based on their standard errors and are used in conjunction with the PDSI sample time series to estimate the mean Poisson rate over the preinstrumental record. This process is repeated 1000 times to generate 1000 sample time series of the prehistoric mean Poisson rate. At each time step, the median value of these sample time series is shown in Figure 8, along with 90% confidence bounds.

The reconstruction for the L.A. gage shows large fluctuations in the average rate of occurrence of extreme precipitation over the 500 year record, with many of the highest risk years occurring in the instrumental (post-1895) and historic (post-1800) record (1884,1868,1941,1983, and 1998). This suggests that years with abnormally high numbers of extremes were no more likely in the prehistoric versus historic and instrumental periods. It is noteworthy though that the prehistoric record contains several multidecadal periods during which the likelihood of extremes has risen above the stationary Poisson estimate based on the instrumental record. By contrast, none of the top nine highest risk years at the Dallas gage occur after 1900, and only two occur after 1800, suggesting that prehistoric extreme precipitation occurrences are likely to have exceeded instrumental (post-1895) and historic (post-1800) levels. The frequent occurrence of high-risk years in the prehistoric record could indicate that the record east Texas floods of May–June 2015 may not be inconsistent with past extreme events for the region.

Finally, a wavelet analysis is used to examine the time-frequency structure of the prehistoric mean Poisson parameter to characterize the low-frequency variability of reconstructed extreme precipitation occurrences at both sites (Figure 9). The Poisson rate is first log-transformed prior to wavelet transform in order to remove any discontinuities due to high skew in the reconstructions, although the major features are unchanged if the raw reconstructions are used. A 16–32 year oscillation in L.A. extreme precipitation

average occurrence rate stands out as the most prominent feature of the two gages. Interestingly, this decadal fluctuation appears intermittently throughout the prehistoric record, emerging between 1700–1800 and 1850–1950, but absent otherwise. In the last 50 years of the record, the L.A. gage also exhibits a 2–7 year signal very similar to that seen in the wavelet spectrum of the original POT data (not shown), but this signal is not consistent throughout the prehistoric reconstruction, suggesting that the influence of ENSO, at least in this frequency band, may be intermittent. The Dallas gage exhibits less low-frequency variability at lower bands than seen for the L.A. gage. However, it does show intermittent oscillations with a 2–8 year period throughout the record that are similar to the power spectrum of the original POT data (not shown), perhaps suggesting weak links with ENSO.

5. Conclusions

This study examined the potential to use the LBDA to reconstruct the frequency of extreme precipitation across the contiguous United States. We first investigated the seasonality and total moisture contribution of extreme precipitation across the country, showing that extreme precipitation accounts for a large portion of total precipitation across much of the western United States, with particularly high contributions in the southwest but also across much of the Great Plains. Extremes in those regions tend to cluster in particular seasons (winter and summer) that are important for moisture availability for tree growth, while extremes are more diffuse across the year in the east. The seasonality and high moisture contribution of extremes in the west suggested that they likely relate to the overall moisture availability needed for tree ring growth, which was confirmed through correlation analyses with both the instrumental PDSI and LBDA.

EOFs were then used to explore the joint spatiotemporal structure of the POT and LBDA data and were compared against REOFs and archetypes to assess their fidelity. The primary mode of variability of both LBDA and POT data sets related remarkably well, with a core center over the southwest and time-frequency structure that resembled the inter-annual and decadal fluctuations of ENSO [*Trenberth et al*., 1988; *Piechota and Dracup*, 1996; *Gershunov and Barnett*, 1998; *Barlow et al*., 2001; *Goodrich*, 2007].

Finally, generalized linear models were used to reconstruct the average rate of extreme precipitation occurrence over the 500 year prehistoric record at two precipitation gages in Los Angeles, CA, and Dallas, TX, based on the local LBDA. The variability and time-frequency behavior of these reconstructions showed a large degree of variability in extreme precipitation occurrences across the prehistoric record, with intermittent structured oscillations with periods ranging from approximately 2–30 years.

While the potential benefits of the LBDA for extreme precipitation reconstruction are promising, there are also several limitations that can hinder its use. As shown in the analysis, the utility of the LBDA for predicting past extremes is only useful in certain areas of the country, particularly arid and semiarid regions in the west, and may be limited by the availability of tree ring chronologies in certain locations. Furthermore, the LBDA cannot be used to identify specific extreme events and the reconstructions presented here instead reflect the likelihood of extremes in any given year. The reconstructions were derived using statistical models fitted over the instrumental record to link the occurrence of extremes to the LBDA. Hence, the fidelity of these reconstructions are based on the assumption of stationarity in these statistical relationships over centennial time scales. Nonstationarity could be introduced through changing characteristics of extremes (e.g., seasonality and percentage of total moisture contribution) that alter how they influence tree growth. The availability of evidence needed to determine whether these characteristics have changed over time may be limited. Furthermore, while we demonstrated as proof of concept the possibility of reconstruction at two grid cells in the southwest and Southern Plains, we have not yet developed a robust approach for predictor selection from the LBDA data and the associated uncertainty analysis.

Future work will explore whether the predictive framework can be extended to extreme event magnitudes and improved if the LBDA is customized for specific months (e.g., September) that maximize skill. Additional research is also needed to examine the hypothesized role of extreme winter precipitation events as a bridge between wintertime Ocean-atmosphere conditions and the summertime LBDA. Finally, extensions to the analysis of floods and their relation to the PDSI will also be explored, with a focus on integrating different sources of paleoflood evidence into a comprehensive statistical framework. A nonstationary paradigm is of particular interest in order to facilitate inter-annual or decadal forecasts of extreme event risk most relevant for planning and management decisions. One possibility is time series models calibrated to the long records

of the LBDA and initialized with current states that explicitly account for and forecast structured inter-annual and decadal oscillations (i.e., Wavelet Auto-Regressive Models [*Kwon et al*., 2008]) that can be extended via statistical link functions to extreme event frequency analyses. Long-range forecasts of ENSO or other ocean signatures (PDO, AMO) developed through recent decadal climate forecast efforts [*Meehl et al*., 2014] could be integrated into this framework. A portfolio of risk management measures (e.g., structural improvements, CAT Bonds, and insurance contracts) could be tailored to these inter-annual or decadal projections for improved protection and economic efficiency.

Acknowledgments
The PDSI and LBDA data for this paper are made available by the National Climatic Data Center. Data set names: Palmer Drought Severity Index and Living Blended Drought Atlas (http://www.ncdc.noaa.gov/paleo/pdsi.html). The daily precipitation at the two gaging stations used in this analysis can also be found at the National Climatic Data Center. Data set names: Global Historical Climatology Network. The gridded precipitation data set, SSTAs, and Niño 3.4 index are available separately through NOAA's Earth System Research Laboratory Physical Sciences Division. Data set name: CPC Unified Gauge-Based Analysis of Daily Precipitation over CONUS; Kaplan Extended SST v2; Climate Indices - Niño 3.4. S. Steinschneider was supported through funding from the NOAA Climate and Global Change Fellowship Program. M. Ho and U. Lall were supported by an award through the National Science Foundation (project EAR-1360446). U. Lall was also supported by an IPA from the U.S. Army Corps of Engineers. We would like to acknowledge the comments of three reviewers and the Associate Editor, which helped to materially improve the article. Lamont-Doherty Earth Observatory Contribution No. 8007.

References

Ault, T. R., J. E. Cole, J. T. Overpeck, G. T. Pederson, and D. M. Meko (2014), Assessing the risk of persistent drought using climate model simulations and paleoclimate data, *J. Clim.*, *27*(20), 7529–7549, doi:10.1175/JCLI-D-12-00282.1.

Baker, V. R. (1977), Stream channel response to floods with examples from central Texas, *Geol. Soc. Am. Bull.*, *88*, 1057–1070.

Baker, V. R. (2013), Global late Quaternary fluvial paleohydrology: With special emphasis on paleofloods and megafloods, in *Treatise on Geomorphology*, vol. 9, edited by J. F. Shroder, pp. 511–527, Academic, San Diego, Calif.

Barlow, M., S. Nigam, and E. H. Berbery (2001), ENSO, Pacific decadal variability, and U.S. summertime precipitation, drought, and stream flow, *J. Clim.*, *14*(9), 2105–2128, doi:10.1175/1520-442(2001)014 < 2105:EPDVAU>2.0.CO;2.

Benito, G., and V. R. Thorndycraft (2005), Palaeoflood hydrology and its role in applied hydrological sciences, *J. Hydrol.*, *313*(1), 3–15.

Benjamini, Y., and Y. Hochberg (1995), Controlling the false discovery rate: A practical and powerful approach to multiple testing, *J. R. Stat. Soc., Ser. B*, *57*(1), 289–300.

Bukovsky, M., D. Gochis, and L. O. Mearns (2013), Towards establishing NARCCAP regional climate model credibility for the North American Monsoon: Current Simulations, *J. Clim.*, *26*, 8802–8826.

Cayan, D. R., K. T. Redmond, and L. G. Riddle (1999), ENSO and hydrologic extremes in the western United States, *J. Clim.*, *12*, 2881–2893, doi:10.1175/1520-0442(1999)012 < 2881:EAHEIT>2.0.CO;2.

Chan, S. C., E. J. Kendon, H. J. Fowler, S. Blenkinsop, N. M. Roberts, and C. A. T. Ferro (2014), The value of high-resolution met office regional climate models in the simulation of multihourly precipitation extremes, *J. Clim.*, *27*, 6155–6174, doi:10.1175/JCLI-D-13-00723.1.

Chen, M., W. Shi, P. Xie, V. B. S. Silva, V. E. Kousky, R. Wayne Higgins, and J. E. Janowiak (2008), Assessing objective techniques for gauge-based analyses of global daily precipitation, *J. Geophys. Res.*, *113*, D04110, doi:10.1029/2007JD009132.

Cole, J. E., J. T. Overpeck, and E. R. Cook (2002), Multiyear La Niña events and persistent drought in the contiguous United States, *Geophys. Res. Lett.*, *29*(13), doi:10.1029/2001GL013561.

Cook, B. I., J. E. Smerdon, R. Seager, and E. R. Cook (2013), Pan-continental droughts in North America over the last millennium, *J. Clim.*, *27*(1), 383–397, doi:10.1175/jcli-d-13-00100.1.

Cook, B. I., R. Seager, and J. E. Smerdon (2014), The worst North American drought year of the last millennium: 1934, *Geophys. Res. Lett.*, *41*, 7298–7305, doi:10.1002/2014GL061661.

Cook, E. R., D. M. Meko, D. W. Stahle, and M. K. Cleaveland (1999), Drought reconstructions for the continental United States, *J. Clim.*, *12*(4), 1145–1163.

Cook, E. R., and P. J. Krusic (2004), North American summer PDSI reconstructions, IGBP PAGES/World Data Center for Paleoclimatology Data Contribution Series, *Tech. Rep.*, 2004–045, 24 pp.

Cook, E. R., R. Seager, R. R. Heim, R. S. Vose, C. Herweijer, and C. Woodhouse (2010), Megadroughts in North America: Placing IPCC projections of hydroclimatic change in a long-term palaeoclimate context, *J. Quat. Sci.*, *25*(1), 48–61, doi:10.1002/jqs.1303.

Cook, E. R., R. Seager, R. R. Heim, R. S. Vose, C. Herweijer, and C. Woodhouse (2010), Megadroughts in North America: Placing IPCC projections of hydroclimatic change in a long-term palaeoclimate context, *J. Quat. Sci.*, *25*(1), 48–61, doi:10.1002/jqs.1303.

Cronin, T. M. (2010), *Paleoclimates: Understanding Climate Change Past and Present*, 441 pp., Columbia Univ. Press, N. Y.

Cutler, A., and L. Breiman (1994), Archetypal analysis, *Technometrics*, 15(1), 661–675.

Dai, A. (2006), Precipitation characteristics in eighteen coupled climate models, *J. Clim.*, *19*, 4605–4630.

Dai, A. (2013), The influence of the inter-decadal Pacific oscillation on US precipitation during 1923-2010, *Clim. Dyn.*, *41*, 633–646, doi:10.1007/s00382-012-1446-5.

Daloz, A. S., F. Chauvin, K. Walsh, S. Lavender, D. Abbs, and F. Roux (2012), The ability of general circulation models to simulate tropical cyclones and their precursors over the North Atlantic main development region, *Clim. Dyn.*, *39*(7), 1559–1576.

Delgado, J. M., B. Merz, and H. Apel (2014), Projecting flood hazard under climate change: An alternative approach to model chains, *Nat. Hazards Earth Syst. Sci.*, *14*(6), 1579–1589.

Déqué, M., D. P. Rowell, D. Lüthi, F. Giorgi, J. H. Christensen, B. Rockel, D. Jacob, E. Kjellström, M. de Castro, and B. van den Hurk (2007), An intercomparison of regional climate simulations for Europe: Assessing uncertainties in model projections, *Clim. Change*, *81*, 53–70.

Ely, L. L., and V. R. Baker (1985), Reconstructing paleoflood hydrology with slackwater deposits: Verde River, Arizona, *Phys. Geogr.*, *6*, 103–126.

Enzel, Y., L. L. Ely, P. K. House, V. R. Baker, and R. H. Webb (1993), Paleoflood evidence for a natural upper bound to flood magnitudes in the Colorado River Basin, *Water Resour. Res.*, *29*, 2287–2297.

Evans, M. N., S. E. Tolwinski-Ward, D. M. Thompson, and K. J. Anchukaitis (2013), Applications of proxy system modeling in high resolution paleoclimatology, *Quat. Sci. Rev.*, *76*, 16–28, doi:10.1016/j.quascirev.2013.05.024.

Fritts, H. C. (1976), *Tree Rings and Climate*, 567 pp., Academic, N. Y.

Fye, F. K., D. W. Stahle, and E. R. Cook (2003), Paleoclimatic analogs to Twentieth-Century Moisture Regimes across the United States, *Bull. Am. Meteorol. Soc.*, *84*(7), 901–909, doi:10.1175/BAMS-84-7-901.

Gershunov, A., and T. P. Barnett (1998), Interdecadal modulation of ENSO teleconnections, *Bull. Am. Meteorol. Soc.*, *79*(12), 2715–2725, doi:10.1175/1520-0477(1998)079 < 2715:IMOET>2.0.CO;2.

Goodrich, G. B. (2007), Influence of the pacific decadal oscillation on winter precipitation and drought during years of neutral ENSO in the western United States, *Weather Forecasting*, *22*(1), 116–124, doi:10.1175/WAF983.1.

Grinsted, A., J. C. Moore, and S. Jevrejeva (2004), Application of the cross wavelet transform and wavelet coherence to geophysical time series, *Nonlinear Processes Geophys.*, *11*, 561–566, doi:10.5194/npg-11-561-2004.

Groisman, P. Y., R. W. Knight, and T. R. Karl (2001), Heavy precipitation and high streamflow in the contiguous United States: Trends in the twentieth century, *Bull. Am. Meteorol. Soc.*, *82*, 219–246, doi:10.1175/1520-0477(2001)082 < 0219:HPAHSI>2.3.CO;2.
Hannachi, A., I. T. Jolliffe, and D. P. Stephenson (2007), Empirical orthogonal functions and related techniques in atmospheric science: A review, *Int. J. Climatol.*, *27*, 1119–1152.
Heddinghaus, T. R., and P. Sabol (1991), A review of the Palmer Drought Severity Index and where do we go from here?, in *7th Conference on Applied Climatology*, pp. 242–246, Am. Meteorol. Soc., Boston, Mass.
Heim, R., R. Vose, J. Lawrimore, and E. Cook (2007), Putting current North America drought conditions into a multi-century perspective. Part 2: Using the blended product in operational drought monitoring, *Eos Trans. AGU*, 88(52), Fall Meet. Suppl., Abstract 02.
Herweijer, C., R. Seager, and E. R. Cook (2006), North American droughts of the mid to late nineteenth century: A history, simulation and implication for Mediaeval drought, *Holocene*, *16*(2), 159–171, doi:10.1191/0959683606hl917rp.
Higgins, R. W., Y. Yao, E. S. Yarosh, J. E. Janowiak, and K. C. Mo (1997), Influence of the Great Plains low-level jet on summertime precipitation and moisture transport over the central United States, *J. Clim.*, *10*, 481–507.
Jain, S., and U. Lall (2001), Floods in a changing climate: Does the past represent the future?, *Water Resour. Res.*, *37*, 3193–3205.
Jones, P. D., et al. (2009), High-resolution palaeoclimatology of the last millennium: A review of current status and future prospects, *Holocene*, *19*(1), 3–49, doi:10.1177/0959683608098952.
Kendon, E. J., N. M. Roberts, C. A. Senior, and M. J. Roberts (2012), Realism of rainfall in a very high resolution regional climate model, *J. Clim.*, *25*, 5791–5806, doi:10.1175/JCLI-D-11-00562.1.
Kunkel, K. E., K. Andsager, and D. R. Easterling (1999), Long-term trends in extreme precipitation events over the conterminous United States and Canada, *J. Clim.*, *12*, 2515–2527, doi:10.1175/1520-0442(1999)012 < 2515:LTTIEP>2.0.CO;2.
Kushnir, Y., R. Seager, M. Ting, N. Naik, and J. Nakamura (2010), Mechanisms of tropical Atlantic SST influence on North American precipitation variability, *J. Clim.*, *23*(21), 5610–5628.
Kwon, H. H., C. Brown, and U. Lall (2008), Climate informed flood frequency analysis and prediction in Montana using hierarchical Bayesian modeling, *Geophys. Res. Lett.*, *35*, L05404, doi:10.1029/2007GL032220.
Kysely, J., Z. Rulfova, A. Farda, and M. Hanel (2015), Convective and stratiform precipitation characteristics in an ensemble of regional climate model simulations, *Clim. Dyn.*, *46*, 227–243, doi:10.1007/s00382-015-2580-7.
Levish, D. R. (2002), Paleohydrologic bounds: Non-exceedance information for flood hazard assessment, in *Ancient Floods, Modern Hazards: Principles and Applications of Paleoflood Hydrology, Water Sci. Appl.*, vol. 5, edited by P. K. House et al., AGU, Washington, D. C.
Lima, C. H., and U. Lall (2010), Spatial scaling in a changing climate: A hierarchical bayesian model for non-stationary multi-site annual maximum and monthly streamflow, *J. Hydrol.*, *383*(3), 307–318.
Lyon, B., N. Christie-Blick, and Y. Gluzberg (2005), Water shortages, development, and drought in Rockland County, New York, *J. Am. Water Resour. Assoc.*, *41*(6), 1457–1469, doi:10.1111/j.1752-1688.2005.tb03812.x.
Markonis, Y., and D. Koutsoyiannis. (2015), Scale-dependence of persistence in precipitation records, *Nat. Clim. Change*, *6*, 399–401, doi:10.1038/nclimate2894.
McCabe, G. J., M. A. Palecki, and J. L. Betancourt (2004), Pacific and Atlantic ocean influences on multidecadal drought frequency in the United States, *Proceedings of the National Academy of Sciences of the United States of America*, *101*(12), doi:10.1073/pnas.0306738101.
McCabe, G. J., J. L. Betancourt, S. T. Gray, M. A. Palecki, and H. G. Hidalgo (2008), Associations of multi-decadal sea-surface temperature variability with US drought, *Quaternary International*, *188*(1), 31–40.
McNamara, J. P., D. Chandler, M. Seyfried, and S. Achet (2005), Soil moisture states, lateral flow, and streamflow generation in a semi-arid, snowmelt-driven catchment, *Hydrol. Processes*, *19*(20), 4023–4038, doi:10.1002/hyp.5869.
Meehl, G., et al. (2014), Decadal climate prediction: An update from the trenches, *Bull. Am. Meteorol. Soc.*, *95*(2), 243–267.
Merz, B., et al. (2014), Floods and climate: Emerging perspectives for flood risk assessment and management, *Nat. Hazards Earth Syst. Sci.*, *14*, 1921–1942, doi:10.5194/nhess-14-1921-2014.
Namias, J. (1966), Nature and possible causes of the Northeastern United States drought during 1962-65, *Monthly Weather Review*, *94*(9), 543–554.
North, G. R., T. L. Bell, R. F. Cahalan, and F. J. Moeng (1982), Sampling errors in the estimation of empirical orthogonal functions, *Mon. Weather Rev.*, *110*(7), 699–7606.
Palmer, W. C. (1965), Meteorological drought, *Weather Bur. Res. Pap. 45*, pp. 58, U.S. Dep. of Commer., Washington, D. C.
Patricola, C., P. Chang, and R. Saravanan (2013), Impact of Atlantic SST and high frequency atmospheric variability on the 1993 and 2008 Midwest floods: Regional climate model simulations of extreme climate events, *Clim. Change*, *129*(3), 397–411.
Patton, P. C., and D. S. Dibble (1982), Archeologic and geomorphic evidence for the paleohydrologic record of the Pecos River inwest Texas, *Am. J. Sci.*, *82*, 97–121.
Piechota, T. C., and J. A. Dracup (1996), Drought and regional hydrologic variation in the United States: Associations with the El Niño-Southern Oscillation, *Water Resour. Res.*, *32*, 1359–1373, doi:10.1029/96WR00353.
Pritchard, M. S., M. W. Moncrieff, and R. C. J. Somerville (2011), Orogenic propagating precipitation systems over the United States in a global climate model with embedded explicit convection, *J. Atmos. Sci.*, *68*, 1821–1840, doi:10.1175/2011JAS3699.1.
Rajagopalan, B., E. Cook, U. Lall, and B. K. Ray (2000), Spatiotemporal variability of ENSO and SST teleconnections to summer drought over the United States during the twentieth century, *J. Clim.*, *13*(24), 4244–4255, doi:10.1175/1520-0442(2000)013 < 4244:SVOEAS>2.0.CO;2.
Rochefort, R. M., R. L. Little, A. Woodward, and D. L. Peterson (1994), Changes in sub-alpine tree distribution in western North America: A review of climatic and other causal factors, *Holocene*, *4*(1), 89–100, doi:10.1177/09596836940040011.
Ropelewski, C. F, and M. S. Halpert (1987), Global and regional scale precipitation patterns associated with El Niño/Southern Oscillation, *Monthly Weather Review*, *115*(8), 1606–1626.
Sankarasubramanian, A., and U. Lall (2003), Flood quantiles in a changing climate: Seasonal forecasts and causal relations, *Water Resour. Res.*, *39*(5), 1134, doi:10.1029/2002WR001593.
Schubert, S., et al. (2009), A U.S. CLIVAR project to assess and compare the responses of global climate models to drought-related SST forcing patterns: Overview and results, *J. Clim.*, *22*(19), 5251–5272.
Seager, R., and M. Hoerling (2014), Atmosphere and ocean origins of North American droughts, *J. Clim.*, *27*(12), 4581–4606.
Seiler, C., and F. W. Zwiers (2015), How well do CMIP5 climate models reproduce explosive cyclones in the extratropics of the Northern Hemisphere?, *Clim. Dyn.*, *46*, 1241–1256, doi:10.1007/s00382-015-2642-x.
Sillmann, J., V. V. Kharin, X. Zhang, F. W. Zwiers, and D. Bronaugh (2013), Climate extremes indices in the CMIP5 multimodel ensemble: Part 1. Model evaluation in the present climate, *J. Geophys. Res. Atmos.*, *118*, 1716–1733, doi:10.1002/jgrd.50203.
St. George, S., and E. Nielsen (2003), Palaeoflood records for the Red River, Manitoba, Canada, derived from anatomical tree-ring signatures, *Holocene*, *13*(4), 547–555.

St. George, S., D. M. Meko, and E. R. Cook (2010), The seasonality of precipitation signals embedded within the North American Drought Atlas, *Holocene*, *20*(6), 983–988, doi:10.1177/0959683610365937.
Stahle, D., F. Fye, E. Cook, and R. D. Griffin (2007), Tree-ring reconstructed megadroughts over North America since a.d. 1300, *Clim. Change*, *83*(1-2), 133–149, doi:10.1007/s10584-006-9171-x.
Steinschneider, S., and U. Lall (2015), Daily precipitation and tropical moisture exports across the eastern United States: An application of archetypal analysis to identify spatiotemporal structure, *J. Clim.*, *28*, 8585–8602, doi:10.1175/JCLI-D-15-0340.1.
Stone, E., and A. Cutler (1996), Introduction to archetypal analysis of spatio-temporal dynamics. *Physica D*, *96*, 110–131.
Therrell, M. D., and M. B. Bialecki (2015), A milti-century tree-ring record of spring flooding on the Mississippi River, *J. Hydrol.*, *529*, 490–498.
Torrence, C., and G. P. Compo, (1998), A practical guide to wavelet analysis, *Bull. Am. Meteorol. Soc.*, *79*(1), 61–78, doi:10.1175/1520-0477(1998)079 < 0061:APGTWA>2.0.CO;2.
Trenberth, K. E., G. W. Branstator, and P. A. Arkin (1988), Origins of the 1988 North American Drought, *Science*, *242*(4886), 1640–1645, doi:10.1126/science.242.4886.1640.
Walsh, K. J. E., et al. (2015), Hurricanes and climate: The U.S. CLIVAR working group on hurricanes, *Bull. Am. Meteorol. Soc.*, *96*, 997–1017.
Wang, C., S. K. Lee, and D. Enfield (2008), Climate response to anomalously large and small Atlantic warm pools during the summer, *J. Clim.*, *21*(11), 2437–2450.
Wang, H., S. Schubert, M. Suarez, and R. Koster (2010), The physical mechanisms by which the leading patterns of SST variability impact U.S. precipitation, *J. Clim.*, *23*, 1815–1836.
Wang, H., A. Kumar, W. Wang, and B. Jha (2012), U.S. summertime precipitation and temperature patterns following the peak phase of El Niño, *J. Clim.*, *25*, 7204–7215.
Ward, P. J., B. Jongman, M. Kummu, M. D. Dettinger, F. C. Sperna Weiland, and H. C. Winsemius (2014), Strong influence of El Nino Southern Oscillation on flood risk around the world, Proc. *Natl. Acad. Sci. U. S. A.*, *111*(44), 15,659–15,664.
Wilks, D. S. (2011), *Statistical Methods in the Atmospheric Sciences*, 3rd ed., pp. 1–704, Academic, San Diego, Calif.
Woodhouse, C. A., and D. Meko (1997), Number of winter precipitation days reconstructed from southwestern tree rings, *J. Clim.*, *10*(10), 2663–2669, doi:10.1175/1520-0442(1997)010 < 2663:NOWPDR>2.0.CO;2.
Woodhouse, C. A., K. E. Kunkel, D. R. Easterling, and E. R. Cook (2005), The twentieth-century pluvial in the western United States, *Geophys. Res. Lett.*, *32*, L07701, doi:10.1029/2005GL022413.
Xie, P., A. Yatagai, M. Chen, T. Hayasaka, Y. Fukushima, C. Liu, and S. Yang (2007), A gauge-based analysis of daily precipitation over East Asia, *J. Hydrometeorol.*, *8*, 607–626.
Yanosky, T. M. (1983), Evidence of floods on the Potomac River from anatomical abnormalities in the wood of flood-plain trees, *U.S. Geol. Surv. Prof. Pap.*, *1296*, 42 pp.
Zappa, G., L. C. Shaffrey, and K. I. Hodges (2013), The Ability of CMIP5 Models to Simulate North Atlantic Extratropical Cyclones*, *J. Clim.*, *26*, 5379–5396, doi:10.1175/JCLI-D-12-00501.1.
Zwiers, F., et al. (2013), *Challenges in Estimating and Understanding Recent Changes in the Frequency and Intensity of Extreme Climate and Weather Events, Climate Science for Serving Society: Research, Modelling and Prediction Priorities*, pp. 339–389, Springer, Dordrecht, Netherlands, doi:10.1007/978-94-007-6692-1_13.